Calibrated near-forward volume scattering function obtained from the LISST particle sizer

Wayne H. Slade and Emmanuel S. Boss

School of Marine Sciences, University of Maine, Orono, ME 04469

wayne.slade@umit.maine.edu

http://misclab.umeoce.maine.edu

Abstract: The physical nature of particles, such as size, shape, and composition govern their angular light scattering, which is described by the volume scattering function (VSF). Despite the fact that the VSF is one of the most important inherent optical properties, it has rarely been measured in aquatic environments since no commercial instrument exists to measure the full VSF in the field. The commonly used LISST (Laser In Situ Scattering and Transmissometry) particle sizer (Sequoia Scientific, http://www.sequoiasci.com) measures near-forward angular scattering of a laser source ($\lambda = 670$ nm) at 32 logarithmically-spaced photodetectors arranged between 0.08 and 15 degrees and inverts the data to obtain particle size distribution (PSD). In order to calibrate the LISST to provide the near-forward VSF of unknown particle suspensions, we analyzed the scattering of light by polystyrene bead suspensions of known size distributions and composition, and empirically compared it with the results of Mie theory. This (1) allowed us to obtain a set of instrument specific scaling factors needed to retrieve the magnitude of the VSF and (2) provided validation that the shape of the VSF was appropriately obtained.

OCIS codes: (000.2170) Equipment and techniques; (010.4450) Ocean optics; (120.5820) Scattering measurements; (290.5820) Scattering measurements; (290.4020) Mie theory; (290.5850) Scattering, particles.

References and links

1. C.D. Mobley, *Light and Water* (Academic Press, San Diego, 1994).
2. D.J. Bogucki, J.A. Domaradzki, R.E. Ecke and C.R. Truman, "Light scattering on oceanic turbulence," Appl. Opt. **43**, 5662–5668 (2004).
3. X. Zhang, M. Lewis, M. Lee, B. Johnson and G. Korotaev, "The volume scattering function of natural bubble populations," Limnol. Oceanogr. **47**, 1273–1282 (2002).
4. E. Boss, W.S. Pegau, M. Lee, M.S. Twardowski, E. Shybanov, G. Korotaev and F. Baratange, "The particulate backscattering ratio at LEO 15 and its use to study particle composition and distribution," J. Geophys. Res. **109(C01014)**, doi:10.1029/2002JC001514 (2004).
5. C.F Bohren and D.R. Huffman, *Absorption and Scattering of Light by Small Particles* (John Wiley and Sons, New York, 1983).
6. M.I. Mishchenko, L.D. Travis, and A.A. Lacis, *Scattering, Absorption, and Emission of Light by Small Particles* (Cambridge University Press, Cambridge, 2002).
7. C.D. Mobley, L.K. Sundman, and E. Boss, "Phase function effects on oceanic light fields," Appl. Opt. **41**, 1035–1050 (2002).

#9523 - $15.00 USD Received 15 November 2005; revised 30 March 2006; accepted 11 April 2006

8. M.E. Lee and M.R. Lewis, "A new method for the measurement of the optical volume scattering function in the upper ocean," J. Atmos. Ocean. Tech. **20(4)**, 563–571 (2003).
9. T.J. Petzold, "Volume scattering functions for selected ocean waters," Contract No. N62269-71-C-0676, UCSD, SIO Ref. 72–78 (1972).
10. WETLabs Inc. (http://www.wetlabs.com), PO Box 518, Philomath, OR 97370.
11. G.R. Fournier and J.L. Forand, "Analytical phase function for ocean water," in *Ocean Optics XII*, J.S. Jaffe, ed., Proc. SPIE **2258**, 194–201 (1994).
12. Sequoia Scientific Inc. (http://www.sequoiasci.com), 2700 Richards Road, Suite 107, Bellevue, WA 98005.
13. P. Traykovski, R. Latter, and J.D. Irish, "A laboratory evaluation of the LISST instrument using natural sediments," Mar. Geol. **159**, 355–367 (1999).
14. Y.C. Agrawal and C. Pottsmith, "Instruments for particle size and settling velocity observations in sediment transport," Mar. Geol. **168(1-4)**, 89–114 (2000).
15. Y.C. Agrawal and P. Traykovski, "Particles in the bottom boundary layer: concentration and size dynamics through events," J. Geophys. Res. **106(C5)**, 9533–9542 (2001).
16. Y.C. Agrawal, "The optical volume scattering function: Temporal and vertical variability in the water column off the New Jersey coast," Limnol. Oceanogr. **50(6)**, 1787–1794 (2005).
17. Duke Scientific Corporation (http://www.dukesci.com), 2463 Faber Place, Palo Alto, CA 94303.
18. X. Ma, J.Q .Lu, R.S. Brock, K.M. Jacobs, P. Yang, and X. Hu, "Determination of complex refractive index of polystyrene microspheres from 370 to 1610 nm," Phys. Med. Biol. **48**, 4165–4172 (2003).
19. P.W. Holland and R.E. Welsch, "Robust regression using iteratively reweighted least-squares," Comm. Stat.: Theory Meth. **A6**, 813–827 (1977).
20. W.H. Slade, "LISST Calibration Information," (http://misclab.umeoce.maine.edu/code/lisstvsf.html).
21. A. Morel, "Optical properties of pure water and pure sea water," in *Optical Aspects of Oceanography*, N. G. Jerlov and E. S. Neilsen, eds. (Academic, New York, 1974), pp. 1-24.
22. K.J. Voss and E.S. Fry, "Measurement of the Mueller matrix for ocean water," Appl. Opt. **23**, 4427–4439 (1984).

1. Introduction

The fundamental properties that regulate radiative transfer within a body of water are the spectral absorption coefficient $a(\lambda)$ [m^{-1}] and the volume scattering function (VSF) $\beta(\lambda,\psi,\phi)$ [m^{-1} sr^{-1}], where λ is the wavelength of light in a vacuum, and (ψ,ϕ) is the polar direction of scattering with respect to the incident beam traveling in the direction of the *z*-axis, shown in Fig. 1. For a collimated incident beam of spectral radiant power $\Phi_i(\lambda)$ [W nm^{-1}], a fraction $\Phi_S(\lambda,\psi,\phi)$ of the beam is scattered at angle (ψ,ϕ) into a solid angle $\Delta\Omega$. The VSF is then defined as

$$\beta(\lambda,\psi,\phi) = \lim_{\Delta\Omega\to 0}\lim_{\Delta z\to 0}\left[\frac{\Phi_S(\lambda,\psi,\phi)}{\Phi_i(\lambda)\Delta\Omega\Delta z}\right]. \quad (1)$$

For unpolarized light with randomly oriented particles, the scattering is assumed to be azimuthally symmetric about the axis of the incident beam, such that $\beta(\lambda,\psi,\phi)=\beta(\lambda,\psi)$ [1].

The total volume scattering function, $\beta(\psi)$, can be separated into a summation of individual scattering components, usually the sum of pure water (w), salts (s), and particles (p): $\beta(\psi) = \beta_w(\psi)+\beta_s(\psi)+\beta_p(\psi)$. Additionally, the scattering due to turbulence [2] and bubbles [3] may be important terms in some cases. In most natural waters, only the scattering of water, salts,

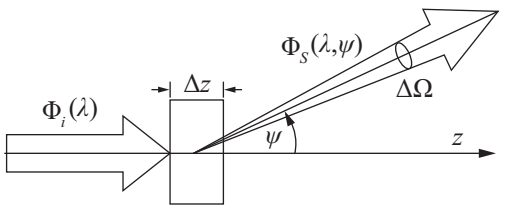

Fig. 1. Incident flux, $\Phi_i(\lambda)$ is scattered within a differential length, Δz, into a solid angle, $\Delta\Omega$. In the figure shown, the scattering is assumed to be azimuthally symmetric about the axis of the incident beam.

#9523 - $15.00 USD Received 15 November 2005; revised 30 March 2006; accepted 11 April 2006

and particles are considered. For the laboratory studies presented here, we are concerned only with pure water and particulate scattering.

The angular distribution of light scattered by particles is governed by the physical properties of the particles themselves, such as size, shape, and composition. The dependence has been demonstrated based on data obtained in situ, in the lab, and modeled using Mie theory and T-matrix methods [4, 5, 6]. As useful as the VSF is for modeling the light field in radiative transfer applications [7] or determining the properties of particles in sea water, it has seldom been measured in the field. The primary reason for the paucity of measurements has been the lack of commercially-available instruments for measuring the VSF in situ due to engineering difficulties [8] and lack of sufficient demand. Only limited measurements of the VSF have been made in the past, with custom-built instruments such as with the General Angle Scattering Meter (GASM) [9]. Lee and Lewis [8] presented a prototype instrument for measuring the complete VSF and reported significant environmental variability in the near-forward VSF. More recently, the use of instruments that measure the VSF at a few angles in the backward direction (such as 100°, 125°, and 150° for the WETLabs ECO-VSF) [10] has become routine.

The scattering coefficient is defined as the integral of the VSF over all angles, assuming azimuthal symmetry,

$$b(\lambda) = \int_{4\pi} \beta(\lambda, \psi, \phi) d\Omega = 2\pi \int_0^{\pi} \beta(\lambda, \psi) \sin(\psi) d\psi. \quad (2)$$

In contrast to the full VSF, the scattering coefficient $b(\lambda)$ [m^{-1}] is routinely measured in situ. It can be computed indirectly by instruments such as the ac-9 [10] as the difference between total light attenuation and absorption. The VSF can be used to estimate the scattering coefficient, since $\beta(\psi)$ is highly peaked in the forward direction, with the majority (69–83% based on VSF observations of Petzold [9]) of particle scatter ($b_p(\lambda)$) contained in $\psi < 15°$. In addition, the near-forward VSF can be combined with measurements from supplementary sensors that measure the VSF at other angles (such as the ECO VSF) to estimate the VSF across a wider angle range by fitting an analytic model (e.g. Fournier-Forand [11])to the measured VSF data using a least squares approach.

The LISST [12] was designed for use in sedimentology to measure the PSD in the field [13, 14, 15]. In the LISST, light from a laser source ($\lambda = 670$ nm) scatters towards a lens on the receiving side of the sample volume, as in Fig. 2. On the other side of the receiving lens is a set of logarithmically spaced concentric ring photodetectors. The lens allows light scattered at a given angle to be collected by a given ring. The 32 photodetector rings are arranged such that their edge radii increase logarithmically, covering a total scattering angle range of approximately 0.08 to 15° in water (note that Sequoia reports the angles in air). There is also a detector at $\psi = 0$ (acceptance angle of 0.0269° in water for the type-B instrument discussed here) used to measure beam attenuation.

Recently, the LISST has been used for quantification of natural variability in the *shape* of the VSF [16]. In the current paper, we present a method to obtain both the shape and magnitude of the near-forward VSF, using Mie theory and lab measurements of polystyrene bead PSD standards to calibrate the LISST-measured angular scattered power to the absolute VSF at near-forward angles.

2. Methods

2.1. LISST measurements

The scattering response of the LISST was related to theoretical calculations of the VSF by analyzing microspheres of a known size distribution and composition. The microspheres were polystyrene particle size standards [17], with diameters ranging from approximately 2 to 100

#9523 - $15.00 USD Received 15 November 2005; revised 30 March 2006; accepted 11 April 2006

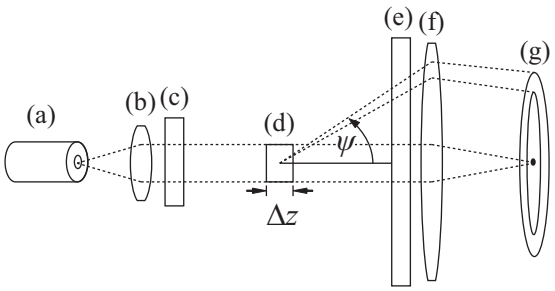

Fig. 2. The LISST has four main optical elements: laser diode source (a), sample volume (d), receiving lens (f), and concentric photodetector rings (g). The laser diode and companion focusing optics (b) provides a collimated beam of incident light ($\lambda = 670$ nm, in air) to the sample volume. The sample volume is separated from the internal optics and electronics by two pressure windows (c and e).

μm, as summarized in Table 1. The EZY-CAL standards were contained in single-use bottles, suspended in water (with trace amounts of dispersant) at an approximate concentration of 2000 particles mL^{-1}. The other standards were contained in dropper-tipped bottles in concentrations on the order of 1% solids by weight. The mean diameters, μ_D, were traceable to the National Institute of Standards and Technology (NIST), evaluated by photon correlation spectroscopy or microscopy using a NIST calibrated stage micrometer. The reported uncertainty in mean diameter, δ_D, for each standard, was the sum of the calibration transfer uncertainty and measurement error. The standard deviation of the size distribution for each standard, σ_D, is certified by Duke Scientific through microscopy or electrical impedance analysis.

We made no independent attempt to validate the manufacturer-provided NIST-traceable particle size distribution. Given the agreement between the theoretical Mie results (which assumes a Gaussian PSD) and the LISST-measured VSF, we must suppose that the single Gaussian PSD is a reasonable assumption. However, users should use caution with such particle size standards, since the dispersant solution used may degrade over time, leading to destabilization of the suspension and aggregation of the beads. Bacterial contamination of the suspension is also possible.

Table 1. Particle size standards used in calibration experiments. μ_D, δ_D, and σ_D are the mean diameter, uncertainty in mean diameter, and standard deviation of microsphere particle size distribution, respectively [17].

Stock Number	Nominal Diameter	$\mu_D \pm \delta_D$	σ_D
4202A	2 μm	2.001$\pm$0.025 μm	0.022 μm
6010 EZY-CAL	10 μm	9.964$\pm$0.058 μm	0.10 μm
4220A	20 μm	20.00$\pm$0.10 μm	0.20 μm
6050 EZY-CAL	50 μm	50.4$\pm$1.0 μm	1.6 μm
4K100	100 μm	99.2$\pm$1.4 μm	1.7 μm

For the calibration experiments, the LISST (LISST-100, type B, s/n 1102) was fitted with a small volume mixing chamber available from Sequoia Scientific [12]. Particle settling was counteracted by recirculating the sample through tubing connected to the sample volume and routed through a peristaltic pump. Turbulence generated due to the recirculation did not have a detectable effect on the optical scattering measured by the LISST, verified by comparing measured results on small beads with and without recirculation. EZY-CAL standards were added

#9523 - $15.00 USD Received 15 November 2005; revised 30 March 2006; accepted 11 April 2006

directly to the chamber in which pure water (Barnstead NANOpure Diamond) was recirculated. Test suspensions were prepared by filling the chamber with pure water and adding microsphere solution directly to the chamber in an addition series. Before additions to the LISST chamber, the sample bottles were agitated by hand or immersed in an ultrasonicated bath.

LISST measurements were logged using the standard LISST-SOP software provided by Sequoia Scientific and further processed in the MATLAB programming environment. Pure water blanks were taken before readings on different microsphere stocks. Blank measurements consist of a set of 32 pure water ring detector outputs, $zscat_i$, where i is the ring detector number, plus clean water laser transmitted power, tr_0, and reference power, ref_0. The raw LISST measurements (32 ring outputs, $scat_i$, laser transmitted power, tr, and laser reference power, ref, for each sample at approximately 1 Hz) were post processed to subtract the pure water ring outputs and for attenuation within the sample volume,

$$cscat_i = \left(\frac{scat_i}{\tau} - zscat_i\right) \cdot dcal_i, \tag{3}$$

where τ is the transmission calculated as $\tau = (tr/ref)(ref_0/tr_0)$, and $dcal_i$ is a set of manufacturer-supplied detector responsivity correction factors. The *zscat* corrected scatter, $cscat_i$ is then corrected for the area of each ring [16], and for laser power in the measurement relative to the clear water measurement, giving the uncalibrated scattered power in each ring, $pscat_i$:

$$pscat_i = cscat_i \cdot \left(\frac{ref}{ref_0}\right) \left(\pi\phi\Delta z(\psi_{i+1}^2 - \psi_i^2)\right)^{-1}, \tag{4}$$

where ϕ is the fraction of a circle covered by the detector and psi_i are the angles (in water) corresponding to edges of the detector rings. Since the 32 detector rings are spaced logarithmically spanning a radius range of 200:1, the edge angles for each ring can be calculated by knowing the inner scattering angle (in air) of the first ring, $psi_{min(air)}$, and correcting for the index of refraction difference between water within the sample volume and air within the instrument,

$$\psi_i = \sin^{-1}\left(\frac{\sin\left(200^{(i-1)/32}\psi_{min(air)}\right)}{m_w}\right). \tag{5}$$

For each calibration run, 1 Hz data were collected and processed according to Eqs. (3)-(4. In order to assess the uncertainty in LISST scattering measurements for a given calibration run, the median, 16th percentile, and 84th percentiles of scattered power were calculated for each ring. Median and percentile values were also calculated for the LISST-measured beam attenuation.

The LISST ring detectors are designed to increase in area geometrically with increasing angle in order to maintain an approximately equal photon flux per area of detector, accounting for the high peak in the near-forward scatter typically observed in natural particle assemblages. For the smallest microspheres, scattering in the most near-forward angles is very low, and due to the variability caused by experimental uncertainty and electronic noise, may lead to negative values of $pscat_i$ (Fig. 3). In order to avoid negative $pscat_i$, for each run used for calibration, we discard rings whose scatter magnitude (median over calibration run) is not sufficiently greater than the variability (half the difference between 84th and 16th percentiles) in $zscat_i$, e.g. $\text{median}(pscat_i)/\delta zscat_i < 10$.

2.2. Theoretical Scattering Response

Mie theory is an exact solution of Maxwell's equations for the interaction of an electromagnetic plane wave with homogenous spheres. Detailed descriptions can be found in Bohren

#9523 - $15.00 USD Received 15 November 2005; revised 30 March 2006; accepted 11 April 2006

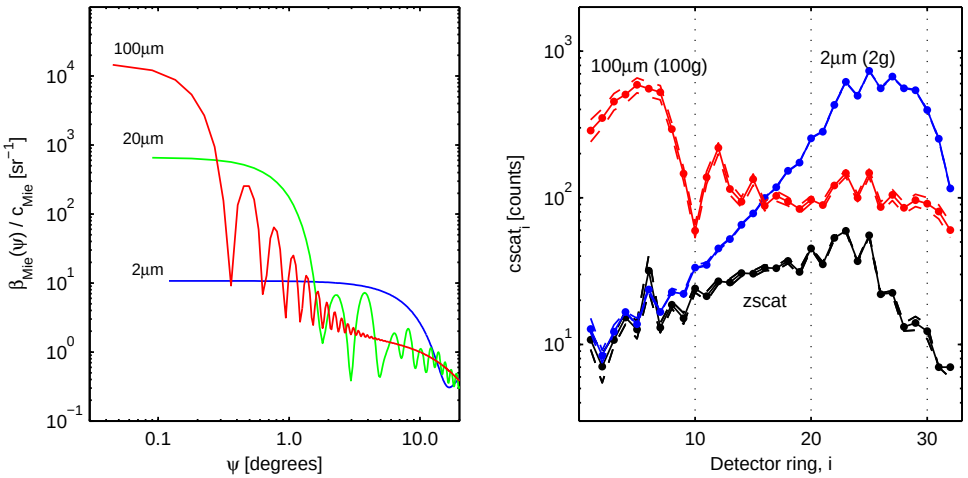

Fig. 3. Plot (a) shows theoretical near-forward VSF of three microsphere standards, derived using Mie theory. The VSF is normalized to beam attenuation. In (b), the raw attentuation-corrected counts, $scat_i/\tau$ for representative 2 and 100 μm calibrations runs are shown along with a pure water *zscat*. Note that for the smaller beads, near-forward detector output is essentially zero, leading to the possibility of negative values of $pscat_i$.

and Huffman [5] and Mishchenko [6]. Mie theory considers wavelength of light, particle size, and particle composition in terms of two fundamental parameters: (1) the size parameter, defined as $x = (2\pi/\lambda)r$, where r and λ are the sphere radius and wavelength of light (in the medium surrounding the particle) and (2) the complex index of refraction of the spheres ($m_p = m'_p + jm''_p$), relative to the surrounding medium (m_w, assumed non-absorbing), $m = m_p/m_w$, where $j = (-1)^{1/2}$. The real index of refraction for polystyrene as a function of wavelength, λ, was calculated based on the results of Ma et al. [18], given in Eq. (6). Imaginary index of refraction for polystyrene ($m''_p \sim \mathrm{O}(10^{-4})$) was not included (see Section 4). The index of refraction of pure water at room temperature and $\lambda = 670$ nm is $m_w = 1.3308$ [1].

$$m'_p(\lambda) = 1.5725 + \frac{0.0031080}{\lambda^2} + \frac{0.00034779}{\lambda^4} \tag{6}$$

For a given x and m, the angular distribution of scattered polarized radiation, $S_1(\psi)$ and $S_2(\psi)$, as well as the scattering, extinction, and absorption cross sections (C_{sca}, C_{ext}, and C_{abs}) were calculated [5].

The size distributions of microsphere calibration standards were assumed to be Gaussian in each case, with the mean diameters and standard deviations provided in Table 1. The general form of the Gaussian distribution is

$$N(D) = N_0 \cdot \tilde{N}(D) = N_0 \cdot \left(\sigma_D\sqrt{2\pi}\right)^{-1} \cdot \exp\left[-\frac{(D-\mu_D)^2}{2\sigma_D^2}\right], \tag{7}$$

where N_0 is the particle concentration [m^{-3}] and $\tilde{N}(D)$ is the size distribution normalized such that $\int \tilde{N}(D)dD = 1$. For each numerical calculation, the assumed distribution was discretized into 200 size bins spanning the range $\mu_D \pm 3\sigma_D$.

#9523 - $15.00 USD Received 15 November 2005; revised 30 March 2006; accepted 11 April 2006

From these quantities, the inherent optical properties can be determined for an assemblage of spheres with known size distribution. For example, particle beam attenuation, c_{Mie}, is calculated by integration of the extinction cross section, C_{ext}, over size distribution,

$$c_{Mie} = \int_0^\infty N_0 \tilde{N}(D) C_{ext} dD. \tag{8}$$

Since concentration varies for each calibration run, attenuation measured by the LISST is used to determine the particle number concentration by normalizing the Mie-calculated values to

$$c^\star_{Mie} = \frac{c_{Mie}}{N_0} = \int_0^\infty \tilde{N}(D) C_{ext} dD. \tag{9}$$

Thus, based on the calculated $c^\star_{Mie}$ [m^2] and the observed c_{LISST}, N_0 is estimated by assuming that $c_{Mie} = c_{LISST}$, hence $N_0 = c_{LISST}/c^\star_{Mie}$. To consider the possible bias introduced by the finite acceptance angle of the LISST transmissometer (0.0269°), the difference between theoretical and measured beam attenuation was determined using $\Delta c = \int_0^{0.0269^\circ} \beta^\star_{Mie}(\psi) \sin(\psi) d\psi$. Based on this formulation, relative bias ($\Delta c/c^\star_{Mie}$) in c_{LISST} was found to be approximately 1.0% for the 100 μm beads, and less than 0.05% for 20 μm and smaller beads.

The phase function, $\tilde{\beta}(\psi)$, was calculated by combining the distributions of scattered power in each polarization,

$$S_{11}(\psi) = \frac{1}{2} |S_1(\psi)|^2 + \frac{1}{2} |S_2(\psi)|^2, \tag{10}$$

and normalizing such that the integral over all angles is unity,

$$\tilde{\beta}(\psi) = \frac{S_{11}(\psi)}{2\pi \int_0^\pi S_{11}(\psi) \sin(\psi) d\psi}. \tag{11}$$

Similar to the case of beam attenuation, the VSF was then determined by integrating over the particle size distribution,

$$\beta_{Mie}(\psi) = \int_0^\infty N_0 \tilde{N}(D) \tilde{\beta}(\psi) C_{sca} dD, \tag{12}$$

and normalized to particle concentration, as in Eq. (9),

$$\beta^\star_{Mie}(\psi) = \frac{\beta_{Mie}(\psi)}{N_0} = \int_0^\infty \tilde{N}(D) \tilde{\beta}(\psi) C_{sca} dD. \tag{13}$$

Figure 3(a) shows the Mie-derived volume scattering functions, normalized to beam attenuation. Note that the VSF for smaller microspheres tend to be less highly peaked for smaller angles. Natural volume scattering functions tend to be more peaked in the forward direction [9], given that they are essentially a superposition of monospecific VSF including particles often larger (and hence their VSF are more forward-peaked) than the 100 μm VSF shown here.

The power sensed by each photodetector ring, i, depends on the integral of the VSF over the angle range of the detector, ψ_i to ψ_{i+1}, so for the purpose of matching LISST-measured scattered power $pscat_i$ for a particular ring to theoretical VSF, we calculated the ring average normalized theoretical VSF as

$$\langle \beta^\star_{Mie} \rangle_i = \frac{\int_{\psi_i}^{\psi_{i+1}} \beta^\star_{Mie}(\psi) \sin\psi d\psi}{\int_{\psi_i}^{\psi_{i+1}} \sin\psi d\psi}. \tag{14}$$

#9523 - $15.00 USD Received 15 November 2005; revised 30 March 2006; accepted 11 April 2006

3. Results

In addition to determination of suspension concentration using measured beam attenuation, two further issues were addressed in the calibration: manufacturer-specified uncertainty in the bead standards and experimental uncertainty in the LISST measurements. A Monte Carlo technique was used to address the reported uncertainty in nominal diameter, δ_D. For each microsphere stock in Table 1, $c^\star_{Mie}$ and $\langle\beta^\star_{Mie}\rangle_i$ were generated for a population of 200 Gaussian size distributions with diameters uniformly varied within the bounds $\mu_D \pm \delta_D$. From the population, the median, 16th, and 84th percentiles (the difference of which is equivalent to twice the standard deviation for normally distributed data) were determined for $c^\star_{Mie}$ and for $\langle\beta^\star_{Mie}\rangle_i$ calculated for each ring.

As discussed in Section 2.1, median values and percentiles were calculated for the LISST $pscat_i$ and beam attenuation. Mie-derived average VSF, $\langle\beta_{Mie}\rangle_i$, was then calculated using

$$\langle\beta_{Mie}\rangle_i = c_{LISST}\frac{\langle\beta^\star_{Mie}\rangle_i}{c^\star_{Mie}}, \tag{15}$$

where c_{LISST} is the LISST-measured beam attenuation. The uncertainty in $\beta_{Mie}(\psi)$ was addressed by propagating the uncertainties in c_{LISST}, $\beta^\star_{Mie}$, and $c^\star_{Mie}$,

$$\frac{|\delta\langle\beta_{Mie}\rangle_i|}{\langle\beta_{Mie}\rangle_i} = \frac{|\delta c_{LISST}|}{c_{LISST}} + \frac{|\delta\langle\beta^\star_{Mie}\rangle_i|}{\langle\beta^\star_{Mie}\rangle_i} + \frac{|\delta c^\star_{Mie}|}{c^\star_{Mie}}, \tag{16}$$

where δc_{LISST}, $\delta\langle\beta^\star_{Mie}\rangle_i$, and $\delta c^\star_{Mie,}$ are the half the difference between the 84th and 16th percentiles of c_{LISST}, $\langle\beta^\star_{Mie}\rangle_i$, and $c^\star_{Mie}$, respectively. For each run used in the calibration (a summary of all runs is presented in Table 2), $\langle\beta_{Mie}\rangle_i$ was calculated according to Eq. (15). The resulting relationship between the theoretical $\langle\beta_{Mie}\rangle_i$ and LISST measurements was assumed linear, and a calibration coefficient [m^{-1} sr^{-1} $count^{-1}$] relating the LISST measured $pscat_i$ to $\langle\beta_{Mie}\rangle_i$ was calculated for each detector ring,

$$\chi_i = \frac{\langle\beta_{Mie}\rangle_i}{pscat_i}. \tag{17}$$

The parameter χ_i for each ring was determined using a robust regression [19] (Fig. 4(a)-(e)). In general, $\delta\langle\beta_{Mie}\rangle_i$ values were small, since changes in VSF due to uncertainty in suspension mean diameter, $\mu_D \pm \delta_D$, and PSD standard deviation, σ_D, were small. Note that accuracy in estimation of the magnitude of $\langle\beta_{Mie}\rangle_i$ is limited by the uncertainty in measuring beam attenuation (e.g. the suspension concentration). For the purposes of determining the χ_i, we used only runs where relative error $\delta c_{LISST}/c_{LISST} < 0.1$. This does not imply that the instrument is not useful in the field when this is not the case, but only ensures relative accuracy in estimating N_0 for the purpose of lab calibration. Smaller beads provide a much flatter scattering response over a wide angle range leading to less averaging error due to $d\beta(\psi)/d\psi$, compared with larger beads with highly variable VSF at larger angles (Fig. 3(a)). Our calibration procedure was to use the 2 μm runs, excluding the first six rings since their $scat_i$ is not sufficiently greater than $zscat_i$ (Fig. 3(b)). Similarly, we added data from 20 μm runs for intermediate rings, excluding rings 15 to 32 since the VSF falls off and fluctuates in this angle range. Data from 100 μm runs were also used since 100 μm beads scatter strongly in the most near-forward rings (Fig. 3(b)), excluding rings 10 to 32 due to fluctuations in the VSF. Our data and MATLAB source code are freely available on our website [20].

The median of calibration coefficients χ_i was $3.1 \cdot 10^{-6}$ [m^{-1} sr^{-1} $count^{-1}$]. Deviation in the largest rings is likely due to increasing $d\beta(\psi)/d\psi$, even for the small 2 μm beads. The error in the model-data fit for each ring (Fig. 4(e)) was calculated as the median relative absolute

#9523 - $15.00 USD Received 15 November 2005; revised 30 March 2006; accepted 11 April 2006

error between the expected Mie-derived ring average scattering and the LISST output for the calibration data,

$$\text{median}\left(|\langle\beta_{Mie}\rangle_i - \chi_i \cdot pscat_i|/\langle\beta_{Mie}\rangle_i\right). \quad (18)$$

Relative error in the χ_i model fit for each ring averaged 6%. Similarly, we calculated the relative absolute error between $\langle\beta_{LISST}\rangle_i$ estimated for the validation data (10 and 50 μm beads, which were not used in deriving the calibration coefficients) and the expected ring averaged VSF based on Mie theory. The validation error (Fig. 4(f)) ranged between approximately 10% and 80%, but was on average 30%. This error is likely an overestimate, since: (1) as in the case of each calibration run, our knowledge of the validation suspension concentration is limited by our ability to measure beam attenuation, (2) our knowledge of the shape of the calculated Mie VSF is limited by our inability to independently verify it (i.e. it is a function of the PSD and the bead properties that we did not verify independently), and (3) the uncertainty is calculated for rings even where our validation beads have complicated fluctuations in their VSF, which would likely not be the case for the VSF of natural waters.

4. Discussion and Conclusion

Our results support the use of the LISST to measure the near-forward volume scattering function of suspended particles. Independent trials using several different sizes of microspheres yielded a set of calibration constants for the detector rings of the LISST, and additional tests on microsphere standards provided an independent consistency check on the calibration. We are unsure of the applicability of the calibration constants derived for the LISST used in this study to other LISST instruments. Variability in the ring-specific χ_i may indicate individual instrument characteristics. Determination of the calibration coefficients depended on knowing the concentration of microspheres within the sample chamber, which we determined using the LISST-measured beam attenuation. Therefore, we used a limited set of experimental runs where the relative error in c_{LISST} was low. We also selected data from particular detector rings for the different size classes of microspheres, since for some runs scatter in particular rings was very low (e.g. Fig 3(b)), and for some bead sizes the VSF was highly variable over particular rings (e.g. Fig 3(a)). A remaining source of uncertainty in the calibration was our assumption of the analytical PSD for the theoretical scattering calculations, which does not account for any destabilization or contamination of the measured suspensions. In the future this uncertainty may be reduced by using PSD measured at the time of calibration.

In the field, the VSF obtained using the derived calibration coefficients includes scattering due to all substances in the sample volume besides that of pure water. This will likely include particles of a variety of different shapes, both single and aggregated, compact and fluffy. The scattering may also include that of colloidal material, salts, turbulence, and bubbles. For a LISST instrument that has been calibrated using pure water *zscat*, in order to determine the total VSF, scatter due to pure water must be added back onto the derived VSF. Volume scattering function due to water can be calculated according to Morel [21], but must be integrated over the ring angle ranges.

The effects of absorption on the Mie-derived VSF in larger angles for larger beads was not negligible, as can be seen in Fig. 6. We avoid these problematic regions of the VSF for the larger, e.g. 20 and 100 μm beads entirely, since (1) errors in calculating the VSF for absorbing spheres may bias calibration data, (2) the VSF is highly variable in these regions leading to possible errors in averaging over ring angles, such as due to error in knowing the absolute ring edges or due to slight misalignment of optical components, and (3) these regions are possibly affected by the polarization of the LISST laser source (discussed below). Coefficients for rings derived using data selected based on these three criteria will possess less uncertainty due to our inability to independently verify the VSF and suspension PSD.

#9523 - $15.00 USD Received 15 November 2005; revised 30 March 2006; accepted 11 April 2006

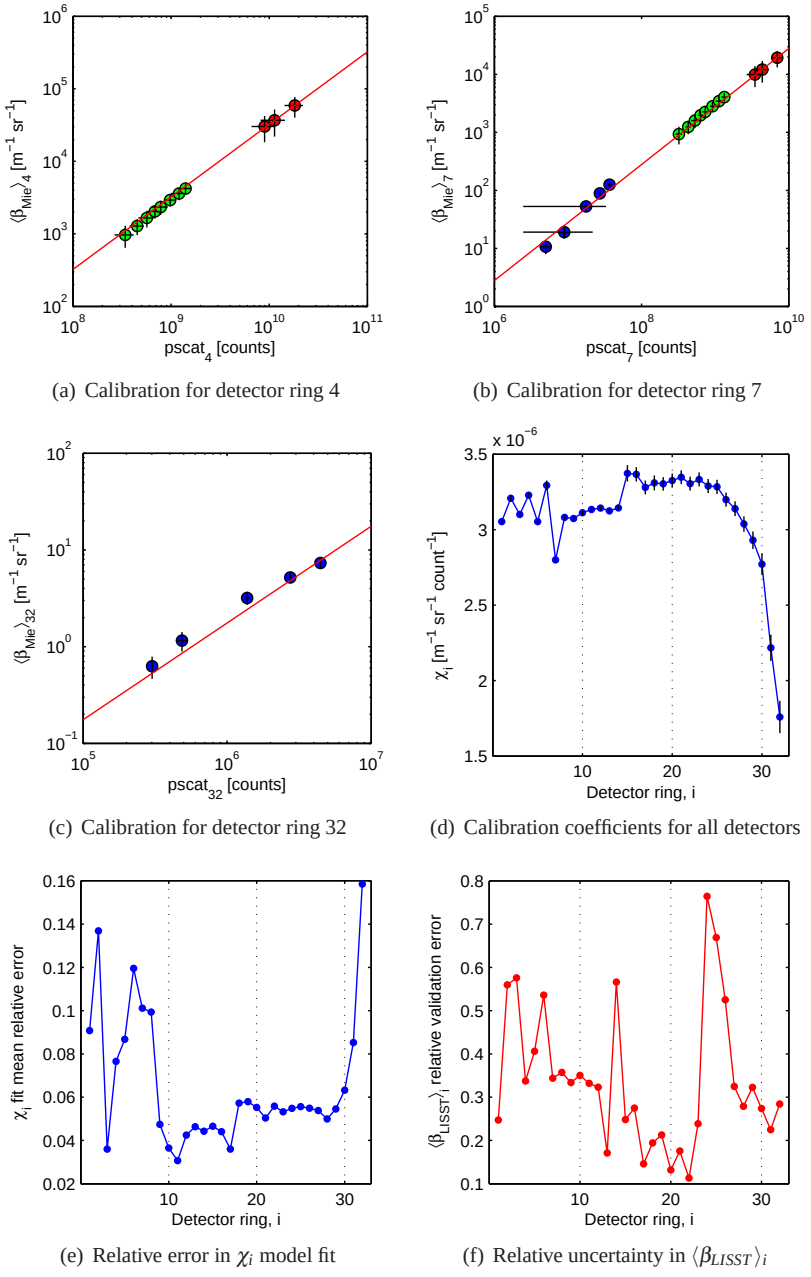

(a) Calibration for detector ring 4

(b) Calibration for detector ring 7

(c) Calibration for detector ring 32

(d) Calibration coefficients for all detectors

(e) Relative error in χ_i model fit

(f) Relative uncertainty in $\langle\beta_{LISST}\rangle_i$

Fig. 4. Plots (a)-(c) show Mie-derived VSF plotted against LISST-measured scatter for three example detector rings. Each data point corresponds to a single run from Table 2; data are marked blue, green, and red, for 2, 20, and 100 μm runs, respectively. Error bars are $\pm 3\delta\langle\beta_{Mie}\rangle_i$ and $\pm\delta pscat_i$. Data are plotted along with the robust fit regression line. In (d) the derived regression coefficients χ_i are shown for each ring, along with error bars $\pm$ the standard error for the coefficient estimates. Plot (e) shows the mean relative absolute error in the χ_i model-data fit for each ring. Plot (f) shows the mean relative uncertainty in VSF estimated for all validation data (10 and 50 μm beads) compared to Mie theory.

#9523 - $15.00 USD Received 15 November 2005; revised 30 March 2006; accepted 11 April 2006

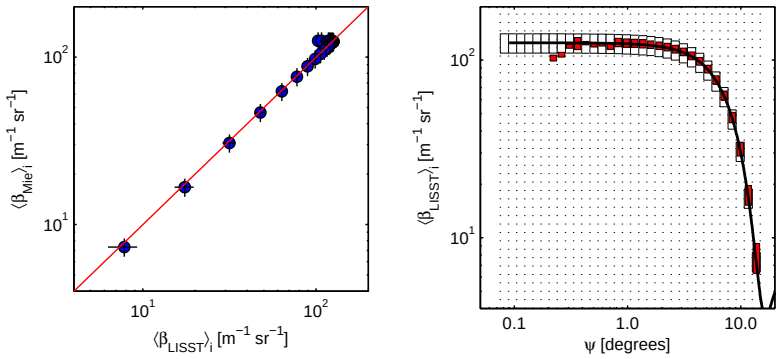

(a) 2 μm run (2f) results

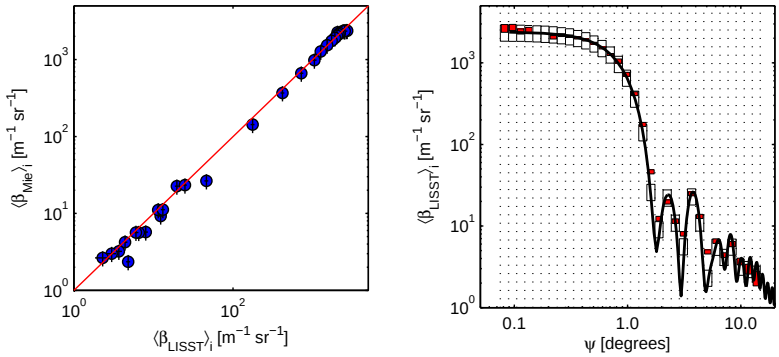

(b) 20 μm run (20h) results

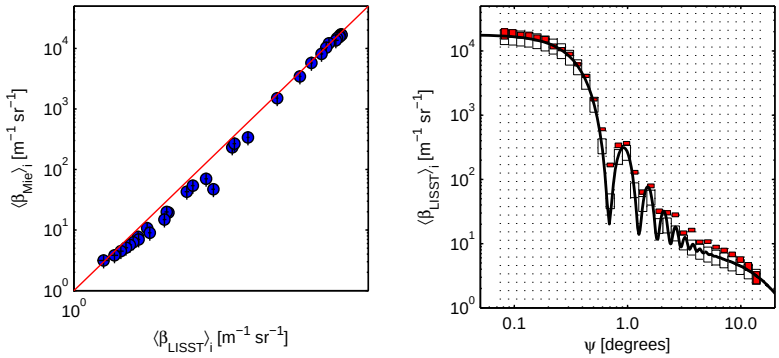

(c) 50 μm run (50c) results

Fig. 5. Three example calibration results for bead runs listed in Table 2. In the left plots, Mie-derived ring-averaged VSF is plotted against calibrated LISST ring-averaged VSF. Vertical error bars are $\pm 3\delta\langle\beta_{Mie}\rangle_i$. Horizontal bars express the LISST-derived ring averaged VSF as 16th and 84th percentile $pscat_i$ values multiplied by $\chi_i - 3\delta\chi_i$ and $\chi_i + 3\delta\chi_i$, respectively, where $\delta\chi_i$ are the standard errors for the coefficient estimates. The solid line is 1:1. In the right plots, calibrated LISST ring-averaged VSF (red filled rectangles) is plotted vs. angle, along with the Mie-derived ring-averaged VSF (empty rectangles) and the continuous VSF (solid line). Dashed vertical lines denote the ring edges. Rings with low signal compared with *zscat* are not shown.

#9523 - $15.00 USD Received 15 November 2005; revised 30 March 2006; accepted 11 April 2006

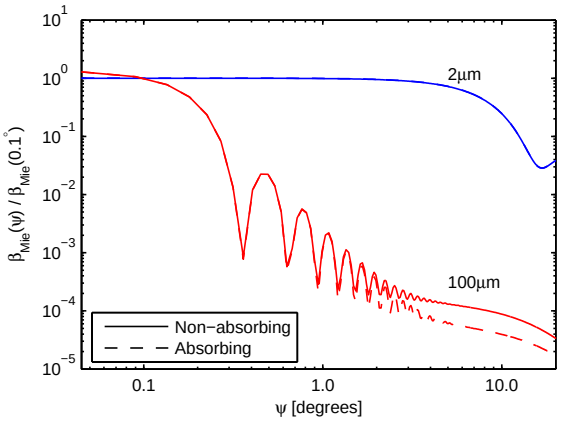

Fig. 6. The effects of including absorption in Mie simulations for 2 and 100 μm microsphere standards. Note that absorbing and non-absorbing cases for the 2 μm beads are indistinguishable in the plot.

The VSF, by definition, describes the scattering distribution of unpolarized light (unpolarized source and detector), namely the S_{11} element of the scattering matrix. However, the LISST source is a collimated laser diode (linear polarized), while the photodetector rings are non-polarized receivers (neglecting any polarization imparted by the optical window and lens). Irradiances measured by such a configuration will incorporate the S_{12} and S_{13} elements of the Mueller scattering matrix [5]. In the case of spherical scatterers, $S_{13} \rightarrow 0$. Figure 7 shows the magnitude of polarization factor, $P(\psi) = -S_{12}(\psi)/S_{11}(\psi)$, calculated using Mie theory for the polydispersions of calibration beads over the angle range of the type-B LISST. This ratio is indicative of the degree of linear polarization of the scattered light, where $|P(\psi)| = 1$ for totally linear polarized light and $P(\psi) = 0$ for unpolarized light. Regardless of the composition or size of spherical scatterers, $P(0^\circ) = P(180^\circ) = 0$. For the suspensions used in this calibration, over the angle range of the type-B LISST, $|P(\psi)|$ is in general less than 0.1, with maximum values in the larger-angle rings. Disagreement between the calculated unpolarized $\langle \beta_{Mie} \rangle_i$ and the polarized LISST-measured scatter could explain some of the deviation in the $\langle \beta_{Mie} \rangle_i$ vs. $\langle \beta_{LISST} \rangle_i$ (or $pscat_i$) relationship for large-angle rings observed in Figs. 4 and 5. For oceanic suspensions the effect of polarization is expected to be even smaller, as $|S_{12}(\psi)/S_{11}(\psi)| < 0.06 \pm 0.02$ and $|S_{13}(\psi)/S_{11}(\psi)| = 0 \pm 0.01$ for the first 20 degrees based on the observation of Voss and Fry [22]. Thus it appears that the errors introduced to the VSF due to the use of a polarized source are small.

This is an exciting time in the field of ocean optics, as for the first time a commercial instrument is available to measure in situ and understand environmental variability in the VSF in near-forward angles. Combining the LISST measurements with other commercially-available sensors measuring the VSF at angles in the backwards direction can provide a means to infer the full VSF, using theoretical VSF models (e.g. Fournier-Forand [11]) to fit measured data, and directly estimate b_p. Knowledge of the full VSF will improve radiative transfer calculation and the associated understanding (through measurements-model comparison) of how ocean color varies in response to changes in the inherent optical properties (e.g. [7]). Comparison with available in-water and bench-top instrumentation will provide the necessary optical closure test for this approach.

#9523 - $15.00 USD Received 15 November 2005; revised 30 March 2006; accepted 11 April 2006

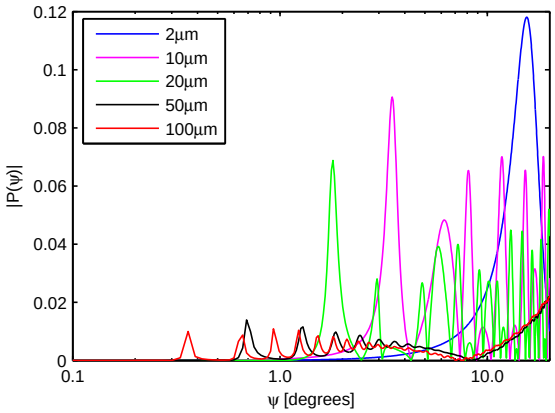

Fig. 7. Magnitude of polarization factor, $|P(\psi)| = |S_{12}(\psi)/S_{11}(\psi)|$ for the microsphere standards, derived from Mie theory.

Acknowledgments

We thank Laura Azevedo for assistance with the measurements. We also thank A. Weidemann and two anonymous reviewers for thoughtful reviews of an earlier version of this manuscript. This work was supported by the Optical & Biological Oceanography program at the Office of Naval Research.

Table 2. Microsphere runs considered in the present analysis. n_{LISST} is the number of scans recorded (at 1 Hz) from the LISST for each run. $c_{LISST}(670)$ and $\delta c_{LISST}(670)$ are the median and relative error of beam attenuation at 670 nm obtained from the LISST during the run. The number concentration of particles, N_0 [m^{-3}], is derived from the LISST attenuation measurements ($N_0 = c_{LISST}/c^{\star}_{Mie}$). The calibration coefficients for the detector rings are determined based on a selection of 2, 20, and 100 μm runs where $\delta c_{LISST}/c_{LISST} < 0.1$, marked (•). Runs marked (✓) were used to validate the calibration coefficients.

Size	Stock	Run		n_{LISST}	$c_{LISST}(670)$	$\delta c_{LISST}/c_{LISST}$	Derived N_0
2 μm	4202A	2a	•	147	4.91	0.02	$4.52{\cdot}10^{11}$
	4202A	2b	•	287	1.78	0.04	$1.64{\cdot}10^{11}$
	4202A	2c	•	126	0.99	0.05	$9.09{\cdot}10^{10}$
	4202A	2d		107	0.38	0.13	$3.52{\cdot}10^{10}$
	4202A	2e	•	101	8.19	0.01	$7.56{\cdot}10^{11}$
	4202A	2f	•	103	11.56	0.01	$1.07{\cdot}10^{12}$
10 μm	6010	10a	✓	40	0.27	0.07	$1.49{\cdot}10^{9}$
	6010	10b	✓	30	0.27	0.07	$1.50{\cdot}10^{9}$
20 μm	4220A	20a		110	0.08	1.02	$1.25{\cdot}10^{8}$
	4220A	20b		131	0.39	0.23	$5.89{\cdot}10^{8}$
	4220A	20c		170	0.91	0.12	$1.36{\cdot}10^{9}$
	4220A	20d	•	132	1.49	0.08	$2.22{\cdot}10^{9}$
	4220A	20e	•	113	1.97	0.05	$2.95{\cdot}10^{9}$
	4220A	20f	•	172	2.55	0.05	$3.80{\cdot}10^{9}$
	4220A	20g	•	122	3.15	0.04	$4.70{\cdot}10^{9}$
	4220A	20h	•	153	3.61	0.04	$5.39{\cdot}10^{9}$
	4220A	20i	•	116	4.51	0.03	$6.73{\cdot}10^{9}$
	4220A	20j	•	134	5.53	0.03	$8.25{\cdot}10^{9}$
	4220A	20k	•	116	6.49	0.02	$9.69{\cdot}10^{9}$
50 μm	6050	50a	✓	303	3.61	0.05	$8.97{\cdot}10^{8}$
	6050	50b	✓	203	2.39	0.06	$5.93{\cdot}10^{8}$
	6050	50c	✓	54	4.44	0.01	$1.10{\cdot}10^{9}$
	6050	50d	✓	40	1.39	0.02	$3.46{\cdot}10^{8}$
100 μm	4K100	100a		86	0.38	0.40	$2.46{\cdot}10^{7}$
	4K100	100b		105	0.67	0.22	$4.27{\cdot}10^{7}$
	4K100	100c		117	0.81	0.24	$5.21{\cdot}10^{7}$
	4K100	100d		145	1.48	0.15	$9.47{\cdot}10^{7}$
	4K100	100e		166	1.89	0.12	$1.21{\cdot}10^{8}$
	4K100	100f		128	2.42	0.12	$1.55{\cdot}10^{8}$
	4K100	100g	•	182	3.45	0.09	$2.21{\cdot}10^{8}$
	4K100	100h	•	153	4.20	0.09	$2.69{\cdot}10^{8}$
	4K100	100i	•	110	6.70	0.06	$4.30{\cdot}10^{8}$

#9523 - $15.00 USD Received 15 November 2005; revised 30 March 2006; accepted 11 April 2006